Simulation of the capabilities of an orbiter for monitoring the entry of interplanetary matter into the terrestrial atmosphere

Alexis Bouquet[a,b,c,d], David Baratoux[c], Jérémie Vaubaillon[e], Maria I. Gritsevich[f,g,h], David Mimoun[i,j], Olivier Mousis[d], Sylvain Bouley[k,e]

[a]*Department of Physics and Astronomy, University of Texas at San Antonio, United States*

[b]*Space Science and Engineering Division, Southwest Research Institute, San Antonio, Texas, United States*

[c]*Université de Toulouse; UPS-OMP; IRAP; Toulouse, France*

[d]*Université de Franche-Comté, Institut UTINAM, CNRS/INSU, UMR 6213, Observatoire des Sciences de l'Univers de Besançon, France*

[e]*Institut de Mécanique Céleste et de Calcul des Ephémérides, UMR8028, 77 Avenue Denfert Rochereau, 75014 Paris, France*

[f]*Finnish Geodetic Institute, Masala, Finland*

[g]*Department of Physical Methods and Devices for Quality Control, Institute of Physics and Technology, Ural Federal University, Yekaterinburg, Russia*

[h]*Department of Computational Physics, Dorodnicyn Computing Centre, Russian Academy of Sciences, Moscow, Russia*

[i]*Institut Supérieur de l'Aéronautique et de l'Espace, Université de Toulouse, France*

[j]*Jet Propulsion Laboratory, Pasadena, California, United States*

[k]*Université Paris-Sud XI, CNRS, Laboratoire IDES, UMR 8148, 91405 Orsay, France*

Abstract

In comparison with existing ground-based camera networks for meteors monitoring, a space-based optical system would escape dependency on weather and atmo-

Email address: alexis.bouquet@gmail.com (Alexis Bouquet)

spheric conditions and would offer a wide spatial coverage and an unrestricted and extinction-free spectral domain. The potential rates of meteor detections by such systems are evaluated in this paper as a function of observations parameters (optical system capabilities, orbital parameters) and considering a reasonable range of meteoroids properties (e.g., mass, velocity, composition) determining their luminosity. A numerical tool called SWARMS (Simulator for Wide Area Recording of Meteors from Space) has been developed. SWARMS is also intended to be used in an operational phase to facilitate the comparison of observations with up-do-date constraints on the flux and characteristics of the interplanetary matter entering our planet's atmosphere. The laws governing the conversion of a fraction of the meteor kinetic energy into radiation during atmospheric entry have been revisited and evaluated based on an analysis of previously published meteor trajectories. Rates of detection were simulated for two different systems: the SPOSH (Smart Panoramic Optical Sensor Head) camera optimized for the observation of transient luminous events, and the JEM-EUSO (Japanese Experiment Module-Extreme Universe Space Observatory) experiment on the ISS (International Space Station). We conclude that up to 6 events per hour in the case of SPOSH, and up to 0.67 events in the case of JEM-EUSO may be detected. The optimal orbit for achieving such rates of detections depends on the mass index of the meteoroid populations. The determination of this parameter appears therefore critical before an optimal orbiting system might be designed for meteors monitoring.

Keywords: Meteors, Photometry

---

1. Introduction

The most widely used method of observation of meteors is through ground-based camera networks (Halliday et al., 1978; Oberst et al., 1998; Trigo-Rodríguez et al., 2004; Jenniskens et al., 2011; Bland et al., 2012). These observations are complemented by multi-instruments aircraft campaigns for meteor shower events (Vaubaillon et al., 2013). A dedicated orbital device would hold considerable advantage over ground-based observations. It would provide wide coverage: for instance, one wide-angle camera with field of view of 120 degrees, at a height of 1200 km would monitor a projected area on the Earth's surface of about 4 millions of km^2. For example, the 60 cameras of the Meteorite Observation and Recovery Project (hereafter "Canadian Network") were distributed over an area of 1.26 millions of km^2 (Halliday et al., 1996). Another advantage is the independence from weather conditions. New scientific perspectives would be also offered such as spectroscopy in a wider spectral domain, including UV, which is not possible from the ground due to the atmospheric absorption. Observations using non-dedicated systems, e.g., from military satellites (Brown et al., 2002), have already demonstrated the feasibility and value of orbital observations. Such systems are also envisioned in the context of interplanetary missions (Christou et al., 2012; Mimoun et al., 2012; Oberst et al., 2012; Koschny and McAuliffe, 2009).

We examine here the performance and scientific return of an Earth-orbiting optical system dedicated to the monitoring of meteors. The detection rate is the primary performance parameter of interest and is evaluated as a function of the characteristics of the monitoring device. A simulator, called SWARMS (Simulator for Wide Area Recording of Meteors from Space) has been developed for this pur-

pose. The detection rate is determined as a function of observation conditions and of the characteristics of populations of meteoroids defined by mass, composition, and entry velocity distributions. Distributions of meteoroids' physical properties are inferred from previous studies. An empirical law relating physical properties to meteor luminosity is derived from an analysis of a set of 259 meteors for which detailed observations (light curve, meteoroid mass, velocity as a function of time) are available. A script, called SAT (Script for Analysis of meteor Trajectories) was developed for this purpose and will be made available upon request to the corresponding author.

The architecture of the software is described in Sec. 2. Section 3 describes SAT and how empirical laws implemented in SWARMS are derived from a set of meteor observations. Populations of meteoroids are described by their mass index. This parameter is varied in the simulations to study its impact on the system performance. The application of SWARMS to two different optical systems, the SPOSH camera and the JEM-EUSO experiment onboard the ISS, are presented in Sec. 4. For the SPOSH camera, the performance of the system is evaluated for different orbits, whereas the ISS orbit is considered for evaluating the performance of the JEM-EUSO experiment. The impact of the assumptions on the population of meteoroids (mass index) is also examined. Section 5 is dedicated to conclusions.

2. A Simulator for Wide Area Recording of Meteors from Space (SWARMS)

2.1. Basic principles of meteor science

All equation parameters with units and definitions are summarized in Table 5. Upon entry into the atmosphere, the kinetic energy E_{kin} of a meteoroid is converted into luminous energy according to the following empirical law relating the instantaneous luminous intensity I (in W) and the rate of kinetic energy loss (Nemtchinov et al., 1994):

$$I = -\tau(t, \rho, ...)\frac{dE_{kin}}{dt}, \tag{1}$$

where τ is the instantaneous luminous efficiency. The instantaneous luminous efficiency may vary with meteor properties and with time. It is then convenient to introduce a global luminous efficiency ($\bar{\tau}$), defined as the ratio between total radiated energy and lost kinetic energy (which in most cases is equivalent to the total initial kinetic energy as the meteoroid rarely reaches the ground). Our simulations use values of global luminous efficiencies and do not consider the details of the meteoroid trajectories. Optical detectors operate in a finite spectral domain, whereas τ and $\bar{\tau}$ are defined as panchromatic quantities. The spectrum of meteor emissions could vary from one event to another and should affect the estimations of τ or $\bar{\tau}$ from optical observations. As the overwhelming majority of meteor spectra available have been limited to the panchromatic visible domain, no definitive conclusion regarding the spectral energy distribution can be drawn. This represents an important source of uncertainty in any simulations using the concept of luminous efficiency.

2.2. SWARMS Specificiations

The three major specifications of the simulator are listed below.

1. A number of assumptions currently made in meteor science may be modified in the future, affecting the calculation of the number and size-distribution of meteoroids, or the estimation of the luminous efficiency from a given meteoroid physical property. New hypotheses or new constraints should be easily implemented.
2. The detector characteristics must be also tunable in order to facilitate the evaluation of the performance of different optical systems.
3. The orbital parameters of the mission must be also tunable. It is indeed expected that trade-off between coverage and distance to phenomena (higher orbit increases coverage but meteors will be farther on average and thus appear fainter) should be routinely done for the purpose of optimization.

2.3. Architecture of the simulator

The general architecture of the simulator is shown in Fig. 1. The algorithm is based on the succession of physical processes leading to meteor detection. We used the Python language to develop SWARMS. The step-by-step calculation of a detection rate for a given situation is given in this section.

2.3.1. Step 1: Generation of the survey area

We describe here how the algorithm determines the field of view of the detector, the corresponding area projected on the terrestrial atmosphere, and how this area is meshed.

Generation of mesh: A mesh representing one hemisphere of the Earth is generated. Each mesh element has the same surface area. The range of latitudes is divided into 200 regular intervals. The range of longitudes is also divided into regular intervals, the number of segments being dependent on the latitude ϕ. The equator (ϕ = 0) is divided into n=1000 segments. For other latitudes the number of intervals is equal to $ncos\phi$ (rounded down). With these parameters, a total number of N =127,924 mesh elements are generated. The coordinates of each mesh element are then converted into a cartesian frame with the origin at the center of the sphere using the average terrestrial radius + 100 km (as meteors usually occur around this altitude).

Discrimination of points in the field of view: The field of view of the detector (Fig. 2) is determined by its orientation (α) with respect to nadir-pointing and aperture (ω). A mesh including only the N_m elements monitored by the detector is extracted from the global mesh. The distance between each point P_i at the center of each mesh element and the detector (O) is then calculated. The surface of the monitored area is given by:

$$S_{monitored} = \frac{N_m(\alpha, \omega)}{N} S, \tag{2}$$

where S is half the surface of the Earth.

2.3.2. Step 2: Generation of physical properties of meteoroids

A population of meteoroids entering the Earth's atmosphere within the field of view of the detector and during a given time of observation is generated at this step. The mass, velocity and density of these meteoroids are randomly assigned from statistical distributions illustrated in Fig. 3.

Generation of masses: The mass-distribution is given as a cumulative distribution function (CDF) providing the number of events above initial mass M_e (initial mass is the mass of a meteoroid before its entry in the terrestrial atmosphere), per unit of time and unit of surface. The main CDF used in this study is given in Sec. 3.2.1. The mass index of a population of meteoroids is the value s such as the number dN of meteoroids with a mass between M and $M+dM$ will be:

$$dN = C_1 M^{-s} dM, \tag{3}$$

where C_1 is a constant. The mass index of the distribution we used is thus 1.48 in the low mass branch. Objects are generated on a selected range of masses (e.g. from 1 μg to 1kg); the lower bound of masses should be chosen based on the lightest detectable meteoroid in order to avoid unnecessary processing of numerous undetectable events. The events are generated through the following steps:

1. The range of masses (expressed by their logarithm) is divided into intervals of the form $[log_{10}M_e,\ log_{10}(M_e\delta)]$, with $\delta = 1+\varepsilon$, ε being a value determined below;
2. the number of events $N_{events,i}$ on the interval i is determined using the CDF;
3. for each interval, a uniform distribution in $\log(M_e)$ is generated. The use of a uniform distribution within the interval introduces an error that depends on the interval width. By comparing total mass given by the CDF and events generated in this way, we found that the error remains below 5% at the condition that $\log(\delta)$ <0.25. The error increases to 10% for $\log(\delta)$=0.5. A value of $\log(\delta)$=0.25 was selected, resulting in a reasonable duration of calculation. A higher mass increases the error. The other value examined

in this study, 2.17, has been tested and yields an error of 6%. This value of error should be investigated if using a higher mass index, and a reduction in the value of $\log(\delta)$ may be necessary.

The number of events in each interval is rounded down. A high-mass interval having a N_{events} value between 0 and 0.5 will therefore not be considered (output of 0 events). This way, the values provided by the simulator are not affected by the possibility of a large event, as the goal is to get typical values to be expected in usual circumstances.

Choosing of speed and density: Velocities V of meteoroids are independently chosen following a Gaussian repartition of logV, reflecting the more frequent occurrence of slow events, as suggested by radar surveys (Hunt et al., 2004). The mean and standard deviation of the function may be easily changed, and other distribution functions may be implemented in the future. The densities (ρ) of meteoroids are independently attributed following a uniform distribution over a density interval (e.g., from 800 kg/m^3 to 4000 kg/m^3) that can be modified.

Spatial distribution of meteors: Meteors are considered to appear with a uniform probability over the monitored area. For each event, an elements of the mesh over the field is randomly chosen and the associated distance to the detector is added to the list of the meteor's properties. The list of meteors' properties also includes kinetic energy and size. For instance, for a 100 000 km^2 surface monitored during 100 hours, with a mass distribution from 0.001g to 1kg, the simulator generates 63 events, that will or will not be detected (As a function of other hypotheses as

per Sec. 4.1).

2.3.3. *Step 3: Determination of luminous efficiency* $\bar{\tau}$

In this step, the global luminous efficiency $\bar{\tau}$ is calculated from the assigned meteoroid properties. The empirical law to calculate $\bar{\tau}$ is determined through the analysis of the Canadian Network meteors (see Sec. 3). The law requires the knowledge of the meteoroid ablation coefficient σ and of its velocity V (Revelle and Ceplecha, 2001). The ablation coefficient σ is calculated from meteoroid density using an empirical inverse-exponential function (see Sec. 3.3).

2.3.4. *Step 4: Detection*

The kinetic energy and luminous efficiency, calculated in step 2 and 3, respectively, are used to calculate the total luminous energy released by a given event. Then, the minimum detectable luminous intensity I_{min} is deduced from the maximum apparent magnitude detectable by the system and the distance from the event to the system. An event is considered to be detectable if its total energy is sufficient to maintain a luminous intensity above I_{min} for the time necessary to appear on a minimum number of frames n_{frames} (set by user). The total energy necessary to fulfill this condition, assuming a steady emission, is given by:

$$E_{min} = I_{min} t_{frame} n_{frames}, \tag{4}$$

with t_{frame} being the duration of exposition for one frame. The above calculation assumes that the meteor light emission is steady during the event duration, which is not the case. The shape of the light curve has to be taken into account; it is possible to approximate light curves as a Gaussian function of reduced time. We

thus determined a factor F to apply on total luminous energy, so that a gaussian profile of light curve featuring a total energy of $F \times E_{min}$ would be visible for as long as a constant emission with a total energy of E_{min}. Thus, equation (4) becomes:

$$E_{min} = I_{min} t_{frame} n_{frames} F \tag{5}$$

The factor F is obtained from a study of a large set of meteors, for which light curves are available, by calculating the average width of the Gauss curve fitted to the light curve (see Section 3.3). In order to determine an average shape of those curves with very different durations, we traced each curve as a function of a reduced time t_r given by:

$$t_r = \frac{t}{t_{total}}, \tag{6}$$

where t_{total} is the total duration of the meteor.

3. Analysis of meteors - SAT

3.1. Basic differential equations

The main equations affecting the evolution of the meteoroid and its trajectory are the drag equation (7) and ablation equation (8) controlling respectively the change of mass and velocity (Nemtchinov et al., 1994):

$$M \frac{dV}{dt} = -0.5 \rho_{atmos} V^2 S c_d, \tag{7}$$

$$H^* \frac{dM}{dt} = -0.5 \rho_{atmos} V^3 S c_h, \tag{8}$$

where M is the mass of the meteoroid, V its speed, ρ_{atmos} is the density of the atmosphere, H^* is the enthalpy of destruction (required to ablate/erode a unit mass

of meteoroid), c_h is a heat transfer coefficient, S is the cross sectional area of the meteoroid, and c_d a drag coefficient. Acceleration due to gravity is neglected in equation (7). Indeed, drag is at least an order of magnitude higher than gravity for a 10cm-sized object of 3500 kg/m^3 density at a typical velocity of 20 km/s. As the object quickly loses altitude, drag rises by several orders of magnitudes with air density (e.g.: 3 orders of magnitude between 120 and 80 km height).

On the other hand, variations of height h above ground are given by:

$$\frac{dh}{dt} = -V sin\gamma, \tag{9}$$

where γ is the slope of the trajectory (with respect to the horizon), assuming a linear trajectory during the meteor phase.

3.2. Mass distributions from the Canadian Newtork

3.2.1. Photometric and dynamic masses

Until more elaborated models were developed (see following section), assessment of mass was done from the luminous intensity (photometric mass) or from the deceleration of the meteoroid (dynamic mass). The two methods are described by Halliday et al. (1996) and applied to the Canadian Network meteors.

The photometric mass is determined by considering that a constant fraction of the initial kinetic energy is converted into luminous intensity (using the concept of global luminous efficiency, $\bar{\tau}$). If $\bar{\tau}$ is known, the deduction of the initial kinetic energy is straightforward and, if the initial velocity is known, the initial mass can be easily determined. Values for $\bar{\tau}$ have been determined from masses constrained

from meteorite recovery (Halliday et al., 1981) or from infrasonic observations (Brown et al., 2002). However, $\bar{\tau}$ may vary over several orders of magnitude as a function of meteoroid properties and the use of a single and constant value for $\bar{\tau}$ is likely to be incorrect (Revelle and Ceplecha, 2001). Moreover, analysis through other means (Sec. 3.2.2) indicates that the photometric method may greatly overestimate the mass, by as much as three orders of magnitude (Gritsevich and Stulov, 2006).

Alternatively, the (dynamic) mass of the meteoroid at a given time may be deduced from equation (7) if the velocity V and the deceleration $\frac{dV}{dt}$ are known. This requires some assumptions on the shape of the meteoroid (governing the values of S and c_d) and on its bulk density. Assumptions on shape (typically spherical or brick-like) are not easily justified. Bulk density varies with both composition and porosity of the body. Another problem is related to fragmentation as dynamical mass assessment applies to the most visible fragment. Moreover, the precise measurement of instantaneous deceleration is difficult, and some meteors show little to no deceleration (1/3 of meteors in Halliday et al. (1996)) and thus their dynamic mass cannot be computed.

The mass-distribution of objects entering the Earth's atmosphere has been determined from photometric masses of the events monitored by the Canadian Network and can be represented with the two following cumulative distribution functions (Fig. 3):

$$\begin{cases} \log N = -0.48 \log M_e + 3.3, with M_e < 2.4 \text{ kg} \\ \log N = -1.06 \log M_e + 5.26, with M_e > 2.4 \text{ kg} \end{cases} \tag{10}$$

where N is the number of objects with initial mass above M_e, in grams, per year

and million of km^2 (Halliday et al., 1996).

3.2.2. *Mass from trajectory analysis*

More accurate but also more complex methods, taking into account erosion, ablation and fragmentation phenomena, offer a better initial mass determination (Ceplecha and Revelle, 2005). However, this kind of analysis requires precise photographic data and observations of fragmentation events. It explains the discrepancies between photometric and dynamic masses by taking fragmentation variation of τ into account. However, as it requires detailed analysis of each meteor (including light curves and photography) it is not appropriate here. Another method, more easily automated, was recently proposed (Gritsevich, 2009a; Gritsevich and Koschny, 2011). This method is entirely based on the interpretation of variations of speed and height as consequences of braking and mass loss (ablation/erosion). The basic equations of meteor physics (equations 7, 8 and 9) are re-written using the following dimensionless parameters:

$$\begin{cases} \overline{h} = h/h_0 \\ \overline{V} = V/V_e \\ \overline{M} = M/M_e \\ \overline{S} = S/S_e \end{cases} \tag{11}$$

where h_0 is the scale height of the atmosphere, M_e the initial mass of the object, V_e the initial velocity, and S_e the initial cross-section. It is assumed that mass and cross section are connected through:

$$\overline{S} = \overline{M}^{\mu} \tag{12}$$

where μ is a coefficient ranging from 0 to 2/3 and representing the effect of the object's change of shape (related to its rotation, which may distribute heat all around the surface and prevents shape change) (Gritsevich and Koschny, 2011). Equation (9) is used in equations (7) and (8) to obtain a system of differential equations of the velocity and mass as a function of height (time is removed). The solution of these equations for the non-dimensional mass and height are given by:

$$\overline{M} = exp(-\frac{\beta}{1-\mu}(1-\overline{V}^2)) \tag{13}$$

$$\overline{h} = ln\alpha + \beta - ln\frac{\Delta}{2}, \tag{14}$$

with:

$$\Delta = E_i(\beta) - E_i(\bar{V}^2\beta), \tag{15}$$

and

$$E_i(x) = \int_{-\infty}^{x} \frac{e^z}{z} dz. \tag{16}$$

The two dimensionless parameters, α and β represent respectively the efficiency of atmospheric braking on the meteoroid, and the efficiency of ablation/erosion of the meteoroid. The expression of these two parameters follow:

$$\alpha = 0.5 c_d \frac{\rho_0 h_0 S_e}{M_e sin\gamma}, \tag{17}$$

$$\beta = 0.5(1-\mu)\frac{c_h {V_e}^2}{c_d H*}, \tag{18}$$

where c_d is the drag coefficient, ρ_0 is the atmospheric density at sea level, S_e is the initial cross-section area of the object. The values of those two parameters α and β can be determined empirically by fitting equation (14) to the trajectory (measured values of $\bar{h}$ and $\bar{V}$). At this stage, no assumption on meteoroid density nor shape has to be done. The ablation coefficient σ and initial mass may be then derived from fitted values of α and β.

The ablation coefficient σ is then defined as

$$\sigma = \frac{c_h}{c_d H*} \tag{19}$$

which is the inverse of enthalpy of destruction multiplied by a factor representing the efficiency with which kinetic energy is converted to heat and transmitted in the material (ratio c_d/c_h). σ can be deduced from β (equation 18) through:

$$\sigma = \frac{2\beta}{(1-\mu){V_e}^2} \tag{20}$$

Previous studies also mentioned a link between σ and density ρ as well as with luminous efficiency τ (Revelle and Ceplecha, 2001). This link is discussed and used in our analysis of the Canadian Network Meteors in Sec. 3.

It is possible to obtain the initial mass M_e through definition of α (see equation 17), with introduction of the shape factor A_e ($=\frac{S_e \rho_m^{2/3}}{{M_e}^{2/3}}$):

$$M_e = (\frac{1}{2} c_d \frac{\rho_0 h_0}{\alpha sin\gamma} \frac{A_e}{{\rho_m}^{2/3}})^3 \tag{21}$$

This requires an assumption on initial shape A_e, drag coefficient c_d and density (ρ_m) of the meteoroid, but no assumption on other physical parameters such as heat exchange coefficient or enthalpy of destruction. In this equation:

$$I = \tau \frac{dE_{kin}}{dt} = \tau \frac{dMV^2}{dt}, \tag{22}$$

we introduce equation (13) in order to replace M. We then use the definitions of α from equation (17) and β from equation (18) in order to eliminate M_e. It is then possible to obtain an equation that links the luminous efficiency τ at a given time with I (Gritsevich and Koschny, 2011):

$$\frac{\tau (c_d A_e)^3}{{\rho_m}^2} = \frac{16 I \alpha^3 sin\gamma^2}{{\rho_0}^3 {V_e}^3 {h_0}^2 f(\bar{V})} \tag{23}$$

where f($\overline{V}$) is a function of the dimensionless velocity:

$$f(\overline{V}) = \overline{V}^3 [E_i(\beta) - E_i(\beta \overline{V}^2)] (\frac{\beta \overline{V}^2}{1-\mu} + 1) \exp(\beta \frac{\mu \overline{V}^2 - 1}{1-\mu}) \tag{24}$$

Therefore, τ may be determined with equation (23) thanks to measured or empirically determined parameters (I, $\bar{V}$, V_e, γ, β, μ), with assumptions on values of $c_d A_e$ and ρ_m.

To summarize, this method can be used to infer the initial mass, luminous efficiency and the ablation coefficient from a least-squares adjustment of the luminosity and velocity observations to the solution of the equations of atmospheric entry. Three input parameters need to be known:

- $c_d A_e$: Unless the shape of the object is known a priori (exceptional case, e.g., Ayers et al. (1970)) or a meteorite can be retrieved and provide some hints on the original pre-atmospheric body (Gritsevich, 2008), it can only be assumed. Example of values found in meteor science are: 1.21 for a body with an initial spherical shape, 1.55 as in Halliday et al. (1996) or 1.65 used

in Verniani (1966) for non perfectly spherical shape, and 1.8 for a brick-like shape (Gritsevich and Koschny, 2011), or $c_d A_e$ = 1.1 considering a small c_d for a spherical body (Wetherill and Revelle, 1981; Revelle and Ceplecha, 2001).

- Bulk density of the meteoroid ρ_m: unless a meteorite can be retrieved, it must be deduced from mechanical properties such as ablation coefficient σ or be assumed. A typical value of 3500 kg/m^3, corresponding to the chondritic density without porosity is often used.

- μ: By using equations (23) and (24) it is possible to obtain μ by fitting the measurement of $I(t)$ to:

$$I = \tau \frac{M_e {V_e}^3 sin\gamma}{2h_0} v^3 (E_i(\beta) - E_i(\beta v^2))(\frac{\beta v^2}{1-\mu} + 1) exp(\beta \frac{\mu v^2 - 1}{1-\mu}) \quad (25)$$

Further details of the method, justifications and example of applications may be found in Gritsevich (2007); Gritsevich and Koschny (2011). A very useful example of application of this method is proposed in Gritsevich et al. (2012).

3.3. Script for Analysis of meteors Trajectories - SAT

This script we have created is intended to process a dataset of meteors including for each time step the time, the height in kilometers above sea level, the velocity in km/s, the absolute magnitude of the meteor (the distance of reference for definition of absolute magnitude of a meteor is 100 km), and the estimation of photometric mass. Deceleration and other values that can be inferred from this

set of observation (dynamic mass, density) are added for time steps for which deceleration could be measured. The data is to be entered in csv format.

The following parameters are calculated directly from the data by SAT:

- *Duration* is used to create dimensionless time steps; average duration of meteors is an indication on possible sampling bias (towards longer events due to slow shutter rotation on the cameras of the Canadian Network);
- *Minimum magnitude* is the minimum absolute magnitude reached by the object,
- *Constant speed* is a Boolean variable to indicate meteors with no apparent deceleration, in order to assess their number and exclude them from analysis requiring deceleration values;
- γ is the slope of the trajectory, with respect to the local horizon, calculated step-by-step from velocity, time and height;
- *PdynInit* is dynamic pressure at the beginning height (first detection) of the meteor. It is calculated from height, velocity, and air density as given by the COSPAR International Reference Atmosphere (CIRA) model (retrieved on British Atmospheric Data Center website in its NetCDF form, more adapted to use with a Python code). This value may be related to mechanical properties of the material;
- *Accumulated energy at beginning height* is the energy accumulated through air friction from the entry in the atmosphere to ignition and could be related

to material properties (Borovička et al., 2007). It is calculated according to:

$$E_s = \frac{1}{2} c_h \frac{V^2}{sin(\gamma)} \int_{h_{init}}^{\infty} \rho_{atmos}(h) dh \tag{26}$$

- *Luminous intensity* is deduced from absolute magnitude in panchromatic domain M_{pan} (through $I = 10^{-0.4 M_{pan} + 3.185}$(Ceplecha and Revelle, 2005)) as a function of time;
- *Total luminous energy* E_{lum} is obtained through integration of Luminous intensity over time;
- An *estimation of the luminous efficiency* $\overline{\tau}$ can be calculated using just the total luminous energy with the relation from Brown et al. (2002):

$$\overline{\tau} = 0.1212 {E_{lum}}^{0.115} \tag{27}$$

  We calculate this value in order to compare the result with values obtained from other methods;
- The *standard deviation of the Gaussian curve* fitting the light curve of the meteor is obtained through least-squares fitting. This information is needed for statistical assumptions on shape of the light curve of a meteor (see equation 5), and thus to determine the factor F (see Sec. 2.3.4).

We have then implemented the method described in Sec. 3.2.2. While α, β and estimation of masses had already been obtained (Gritsevich, 2009b) for the set of Canadian Network meteors analyzed in Sec. 3.4, the implementation into SAT allows to perform the calculations with different assumptions (for mass estimation) and combine them with the latest development of the method: the determination

of τ as in Gritsevich and Koschny (2011). The determination of mass and luminous efficiency requires assumption on the density ρ_m. This has been achieved by inferring ρ_m from ablation coefficient σ. Values determined in Revelle and Ceplecha (2001) have been used, coming from analysis of a sample of events for which precise trajectory measurements were available. As those values are determined for four groups (and thus represent four couples ρ_m vs σ) we fitted those values into an empirical inverse-exponential law relating ρ_m to σ:

$$\rho_m = 0.25 + (4.77 \pm 0.17) exp(-(23.5 \pm 1.4)\sigma) \tag{28}$$

The 0.25 value has been arbitrarily fixed to correspond to the apparent asymptotic value of most fragile meteoroids. This law does not account for the fraction of low-σ, high-ρ objects represented by the ferrous meteoroids, for which ρ_m could rise to 8000 kg/m^3. The value of σ is required to get ρ_m and must be deduced from β as seen in Sec. 3.2.2, equation (20). β being empirically fitted and V_e being measured, μ must be calculated. We do so through the least-squares method (see Sec. 3.2.2, equation 25). Through this calculation process, an estimation of initial mass M_e is obtained. From this point, $\overline{\tau}$ may be determined from the initial kinetic energy using M_e and V_e and integration of I for the total luminous energy, or alternatively from an integration over time:

$$\overline{\tau} = \frac{\int_{v_{final}}^{1} \tau(v) M(v) V^2 dv}{\int_{v_{final}}^{1} M(v) V^2 dv} \tag{29}$$

Whereas using equation (29) may detect some problems in velocity measurements[1], it has no special interest and is more complicated, thus we relied on the

[1]Erroneous values of velocity could yield negative $\tau(v)$ values, arguing for the rejection of the

ratio of the integrated luminous intensity to initial kinetic energy. The output file of data processing is a .csv (comma-separated values) file in which global values (as opposed to values for each time step of a meteor) are given for each meteor.

3.4. The Canadian Network Analysis

3.4.1. General consideration on the Canadian Network observations

The result of the application of SAT to the Canadian Network meteors is described here with the objective to establish empirical relationships between the luminous efficiency $\overline{\tau}$ and physical properties of meteoroids. The data of the Canadian Network were selected as it contains a large number of meteors for which all data required for analysis with SAT are available in Halliday et al. (1996). For instance, other data such as the Prairie Network could be used too but need more work to be converted into a usable format from the available pdf. It should be noted that the average duration of Canadian Network meteors is 2.4 s (median value is 1.8 s). This is above the usual average duration of meteors of 0.3 s; due to low shutter rotation speed and sensitivity of cameras, the network is biased towards longer, brighter meteors. Also this set of data was oriented towards higher brightness meteors (hence the use of the "fireball" term). About 1/3 of the meteors (88 out of 259) do not show any measurable deceleration, as either the body's inertia was extremely high, or ablation was predominant (drag causing fragmentation instead of aerobraking the whole body). The former interpretation would imply very low α values for such events. The critical size of the body to appear as non-decelerating with the accuracy of the Canadian Network may be estimated

entire record

from the drag equation (7). Even using the highest density (8000 kg/m^3, corresponding to a ferrous body) a size of 150km would be necessary. Dominance of the ablation mechanism is therefore the favored explanation to non-decelerating meteors. These non-decelerating bodies are not submitted to SAT (Sec. 3.2.2). It should also be noted that this study is biased towards objects with the highest strength. The generally low value of the ablation coefficient found in Sec. 3.4.2 further confirms that. This can explain why it was not possible to distinguish between several groups of meteors based on beginning height or accumulated energy of beginning height, as the majority of meteors of this sample belongs to a single group.

3.4.2. Analysis of meteor trajectories

SAT allowed us to obtain σ and μ values through the methods described in Section 3.3. We note that μ values, when it is possible to estimate this parameter, are generally high, with an average value of 0.56 and in 2/3 of the cases a value of 0.65, corresponding to the upper bound permitted when heat is redistributed by rotation to the whole surface of the body (see Fig. 4). This implies that most meteoroids keep their shape during atmospheric entry. Calculation following the methods of Section 3.3 are achieved to assess the mass of meteoroids. As explained previously, determination of mass permits determination of kinetic energy and thus luminous efficiency, which is used in Sec. 3.4.3. Values of mass calculated in this way may differ from photometric evaluations by as much as 3 orders of magnitude (Gritsevich and Stulov, 2006). However, a comparison of the masses estimated by the two approaches for the Canadian Network meteors did not reveal any obvious trends, the average value of $log\frac{M_{phot}}{M_{trajectory}}$ being 0.24, with a

standard deviation of 1.2; this does not allow to find a correction to apply to the distribution. We thus elected to adopt distributions of events from Halliday et al. (1996) as a reference for SWARMS, using the cumulative distribution function given in Sec. 3.2.1. Another important finding is the low ablation coefficient σ (Fig. 5). While the four groups identified by Revelle and Ceplecha (2001) feature 100σ values spanning a range from 1.4 to 21, most of the values derived here are clustered below 3. The causes of this repartition are difficult to explain. It can be due to the "hardest" meteors (ie, with the lowest ablation coefficient) being the brightest and longest (hence an observation bias from the Canadian Network). Another possibility would be that high values of sigma would be associated with low-strength meteors, having high ablation coefficient, and for which deceleration is too small to be resolved by the Canadian network.

3.4.3. Fitting of Luminous efficiency (τ) law to use in simulator

Following the conclusions of Revelle and Ceplecha (2001), the luminous efficiency $\overline{\tau}$ is considered to be a function of V_e and ablation coefficient σ. The parameters A, B, and C of the following empirical law between $\overline{\tau}$ and σ are determined using least-squares:

$$\overline{\tau} = A(V_e - V_0)^B \sigma^C, \tag{30}$$

where V_0 is chosen at 10 km/s, to represent the absence of emission in the panchromatic range of a body entering at a low velocity. The following law was obtained:

$$\begin{aligned} \ln \overline{\tau} = -5.278 \pm 0.66 + (0.87 \pm 0.26) \ln(V_e - V_0) \\ -(1.46 \pm 0.2) \ln(100\sigma) \end{aligned} \tag{31}$$

with V_e in km/s. We find that τ is an increasing function of V_e. Values of luminous efficiency inferred from this law are mostly in the 0.1% to 3% range. Those values are lower than calculated in previous works for the group of hardest meteors ($\tau = 5.57\%$)(Revelle and Ceplecha, 2001) As a comparison, the law proposed by Brown et al. (2002) yields values all close to 2%. This law has been fitted to bodies large enough for their kinetic energy to be deduced through infrasonic measurements, and may not be applicable to the smaller ones detected by the Canadian Network.

4. Results and discussion

For the following application that considers the performance of available detectors as a function of the orbital parameters, we used both parts of the program described in the previous section. The SAT part, described in Sec.3, allowed us to analyze a sample of meteors to deduce a law linking physical properties to luminous efficiency. It also extracts other quantities that can be used in other analysis. The SWARMS part, described in Sec. 2.2, allows to obtain a number of meteor detection per hour based on the detector used for observation, its positioning, and the assumption on meteoroids (including luminous efficiency law that has been deduced with SAT).

4.0.4. The SPOSH camera

The SPOSH camera (Fig. 6) has been developed specifically for the purpose of observing transient luminous phenomena from orbit (meteors and noctilucent clouds). Its characteristics are detailed in Oberst et al. (2011), the features that

are critical in this study are given in Table 5. Its mass would reach 2.33 kg with a nominal shielding of 3 mm walls (for a 30 krad requirement). The ability to detect an apparent magnitude 6 object moving at $5^\circ/s$ is a specification of the camera. The actual device has proven to be able to detect meteors as faint as magnitude m=5.5 moving at $8^\circ/s$. For simulations we keep the conservative values of the specifications (m=6 at $5^\circ/s$). We performed simulations for SPOSH with different altitudes, from 200 km to 5000 km. The lower value allows to be closer to meteors (and thus to detect fainter ones) at the expense of mission duration (atmospheric drag), coverage, and high angular speed of meteors. Higher altitudes permit wider coverage but reduce the ability to detect fainter meteors. SPOSH is considered at its shortest exposure time (0.06s). Three frames are required for a valid detection.

4.0.5. The JEM-EUSO experiment

The JEM-EUSO experiment (Ebisuzaki et al., 2011) is dedicated to the detection of high-energy particles colliding with the Earth's atmosphere with a detector in orbit, mounted on the ISS (International Space Station). Its launch date is not yet determined. A case has been made for its use in the detection of other phenomena, including meteors (A. Celino, personal communication). The following remarks can be made about this use:

1. The mission profile is fixed (orbit at 400 km on the ISS).
2. The monitoring would be done in the near-UV band: 290 to 430 nm. It is difficult to know what would be the consequence on the rate of detection: meteors may contain a lot of energy in the UV band (Carbary et al., 2004) but the 290 - 430 nm band may be also quite narrow. The difference with

the usual panchromatic monitoring of meteors makes difficult to apply current results to this experience; it is possible that higher energy in this band compensates for its narrowness.

3. The field of view of 60° x 60° provides a considerable coverage, albeit less important than SPOSH.
4. As its primary mission is the monitoring of high-energy particles, JEM-EUSO has to be able to capture very short events in the μs range. Meteors are "slow" events for this device: angular speed of the object is not a concern.
5. Reconstruction of trajectory could be possible for the brightest meteors: triangulation could be done on their persistent trains thanks to the orbital motion of the ISS. We have performed a calculation with this configuration and assuming a persistence of the trail of 1s (conservative assumption as trains can last for minutes). Results show that an angular resolution of 0.2° would be required for triangulating the position of a train segment lasting 1s at the maximum distance (determined with optimal tilt for meteor detection as found in Sec. 4.1).
6. The JEM-EUSO experiment does not feature a spectrometer, precluding the acquisition of meteor spectra.

We have considered the field of view and position (at 400 km) of JEM-EUSO. As there is very few information on the quantity of energy emitted in the near-UV spectrum by meteors, the same requirement on apparent magnitude is held as for visible observations. The requirement on number of frames and duration of exposure (accounted for in the E_{min} calculation) was kept from SPOSH: even though JEM-EUSO has μs exposure time, the time scale of meteor phenomena

(deceleration, evolution of light curve) is still around 0.1s.

4.1. Simulation results

4.1.1. Summary of main assumptions

All our simulations are based on the following assumptions.

- The cumulative distribution function of number of events depending on their mass is taken from the results deduced from Canadian Network observations (Halliday et al., 1996), as seen in Sec. 3.4.2.
- The distribution of density is uniform between 1000 kg/m^3 and 4000 kg/m^3. This distribution includes more low density material than suggested by meteorites recoveries. Meteorite-deduced distributions favor higher values of density due to the toughest materials more often surviving atmospheric entry. Since low density materials have lower luminous efficiency, our chosen distribution tends to lower the expected number of detections and is a conservative choice;
- The distribution of speeds is based on the results of radar surveys, taking into account the bias of detection depending on the speed of entry (Hunt et al., 2004). We elected to use a Gaussian distribution of logV_e, centered on 20 km/s (see Fig. 3).
- Ablation coefficient σ is deduced from density ρ_m through equation (28).
- Global Luminous Efficiency $\overline{\tau}$ is deduced from σ and V_e (see Sec. 3.4.3):

$$\overline{\tau} = 0.0051(V_e - V_0)^{0.87} 100\sigma^{-1.46} \tag{32}$$

deduced from equation (31).

- As explained in Sec. 2.3.4, a coefficient F on the minimum energy E_{min} has to be applied to take the shape of light curves into account. Through calculation of the average shape of the light curves of meteors of the Canadian Network, this coefficient has been found to be equal to 18.51. This means that the actual minimum luminous energy of detection is 18.51 times the energy required to detect a theoretical meteor with steady emission during the minimum required time.

4.1.2. First use case: the SPOSH camera

We have tested a SPOSH camera oriented towards nadir at various altitudes, from 200 km (100 km from the atmospheric layer at which meteor occur, conditions similar to observation from ground) to 5000 km. However, due to the presence of radiation belts, a mission above 1800 km is not possible as the satellite would be damaged and eventually put out of order by high-energy particles. Values above this height are only indicated for illustration purposes. The evolution of coverage is shown in Fig. 7. At an height above ground of 1100 km, SPOSH covers the Earth "horizon to horizon"; past this point, increasing the altitude is less effective at increasing coverage, as the Earth does not fill the whole field of view anymore. The detection rates are represented in Fig. 8. The rate of detections rises with orbit height to reach a maximum at 3000 km above ground, with 6 events per hour implying that increased coverage is more important than proximity. The inflection in the curve at 1100km is due to the less favorable evolution of coverage above this altitude. Above 3000 km, distance causes an important loss of apparent magnitude that prevents the detector from seeing the bulk of the meteoroid population.

4.1.3. *Second use case: JEM-EUSO experiment*

The main difference between SPOSH and JEM-EUSO is the smaller field of view (60° x 60°) of the JEM-EUSO experiment, and the fixed altitude (400 km, altitude of ISS). However, JEM-EUSO may be tilted to increase coverage (but increasing the distance to meteors) so we have simulated different tilt angles, from 0 to 90°. The area covered is roughly 100 000 km^2 when looking towards nadir. Evolution of coverage with tilt angle is given in Fig. 9. The maximum surface area covered is attained a 60° tilt; above that, most of the field of view is above the horizon and thus not suitable for meteor detection. Detection rates are displayed in Fig. 10. Due to the relatively low altitude and coverage, the number of detections remains between 0.1 and 0.67 per hour, the latter being for a 60° tilt. As the distance between meteors and the device stays low, the main factor in the number of detection is the surface area covered, as evidenced by the similar shapes of the curves plotted in Fig. 9 and 10.

4.1.4. *Effect of mass index of meteoroid distribution*

Simulations performed with the distribution deduced from the Canadian Network show that increasing altitude is the best way to maximize the number of detections: wider coverage compensates for increased distance to meteors. However, this conclusion could be altered if a different mass distribution, with a higher mass index, is supposed, as discussed in Sec. 3.2.1. To evaluate how results depend on mass index, we have performed simulations with a mass index of 2.17 deduced from naked-eye meteor counts (Rendtel, 2004):

$$logN = -1.17 logM_e + 2.75 \tag{33}$$

The 2.75 constant is chosen so that at a height of 200 km, close to conditions of observation from the ground, the number of meteor matched an extrapolation of naked eye counts. However, the main interest of this calculation is to observe the change of trend in number of detections depending on observer's height. Results are illustrated in Fig. 11 and clearly show that under this hypothesis, the lowest orbit possible is optimal regarding the number of detections.

It should be observed that the flux we used has been established with a network dedicated to fireballs, so it shouldn't be expected to be accurate at low masses. A distribution established with in-situ detectors of interplanetary dust could be considered instead, such as the one of (Grun et al., 1985). This would imply a mass index of 2.34 (as opposed to 1.48 for Halliday et al. (1996)) at low masses. A combination of the distributions in their respective domains of validity should be considered. Preliminary calculations show that increasing the mass index for bodies below 0.1 g increases the number of detections at low altitude (behavior shown in this section) but that our conclusions are unaffected for an orbit height above 1000km, where the objects below 0.1g are not detected.

5. Conclusions

We have developed SWARMS, a simulator able to predict the number of meteor detections from a space-based dedicated monitoring system. The simulator can take into account different hypotheses on frequency of events, distributions of masses, speeds, and density, on the process leading to light emission. The numerical tool may be easily adapted for different observation conditions (including observations around other bodies of the solar system). The meteor parameters

used in our simulation derive essentially from the analysis of the meteors detected by the Canadian Network from 1974 to 1985. Our deductions are:

1. This sample contains mostly hard (low ablation coefficient) meteoroids. Further analysis by considering alternative datasets would be useful to draw more general conclusions.
2. Estimation of mass through trajectory analysis may differ radically from photometric estimation depending on meteor, but our analysis does not permit to reconsider the distribution proposed by Halliday et al. (1996).
3. We have calibrated a law linking global luminous efficiency to ablation coefficient and initial velocity. We have found that luminous efficiency is best fitted by an increasing function of velocity. This law gives luminous efficiencies mostly in the range of a fraction of a percent to a few percent.

Simulations with the chosen distribution of masses show that maximizing coverage permits a higher rate of detection even if meteor are further and thus fainter. A detector at 1800 km (practical maximum due to radiation belts) should make 5.7 detections per hour, against 0.7 detections per hour at 400 km. Low orbits also raise the question of the life expectancy of the mission. Simulations considering the use of JEM-EUSO experiment show that the reduction of field of view affects the rate of detections in a noticeable way (7 times less detections), however, optimal tilting of the detector (towards the limb) increases the number of detections up to 0.67 detections per hour. Those rates of detection would allow to quickly enrich meteor databases; once the mission is operational, SWARMS could be used to fit models on the number and properties of meteoroids (and models of the meteor phenomenon) to observations. However it appears that different distributions in meteoroids masses (higher mass index, ie distribution shifted towards

higher number of small objects) may reverse the observed trend between the number of detections and the height of the detector. Therefore, a good constraint on the mass index of the target population is critical to decide the optimal height for the mission. This can be achieved thanks to simpler missions dedicated only to meteor counting by nanosatellites (e.g., Charriet and Fayolle (2013)). Next steps to be taken will be to consider the requirements to put on the system for trajectory reconstruction. The practicality and feasibility of reconstructing trajectory from only one point of view (using train persistence and orbital motion of the device) should be studied and could impose new constraints to decide optimal height at which to place the detector. Additionally, the ability to detect the brightest meteors during daytime should be investigated. The ideal mission for the monitoring of meteors should include two satellites featuring a wide-angle camera monitoring UV and panchromatic domains in order to maximize the number of detections and permit trajectory reconstruction. It would also include a spectrometer on one of the satellites, as spectroscopy of meteors (especially in UV domain) shows great promise.

Acknowledgements

This research has been funded by CNES through the grant for the project METEOR. The Partenariat Hubert Curien MA/11/257 is also acknowledged for supporting the presentation of this work to OISA 2013 at Marrakech. IPPW Student Organizing Committee is acknowledged for supporting presentation of this work at IPPW 10. Maria Gritsevich is supported by the Academy of Finland. Thanks to Daria Kuznetsova and to two anonymous reviewers for useful corrections and comments.

References

Ayers, W. G., McCrosky, R. E., Shao, C.-Y., Jun. 1970. Photographic Observations of 10 Artificial Meteors. SAO Special Report 317.

Bland, P. A., Spurný, P., Bevan, A. W. R., Howard, K. T., Towner, M. C., Benedix, G. K., Greenwood, R. C., Shrbený, L., Franchi, I. A., Deacon, G., Borovička, J., Ceplecha, Z., Vaughan, D., Hough, R. M., Mar. 2012. The Australian Desert Fireball Network: a new era for planetary science. Australian Journal of Earth Sciences 59, 177–187.

Borovička, J., Spurný, P., Koten, P., Oct. 2007. Atmospheric deceleration and light curves of Draconid meteors and implications for the structure of cometary dust. Astronomy and Astrophysics 473, 661–672.

Brown, P., Spalding, R. E., ReVelle, D. O., Tagliaferri, E., Worden, S. P., Nov. 2002. The flux of small near-Earth objects colliding with the Earth. Nature 420, 294–296.

Carbary, J. F., Morrison, D., Romick, G. J., Yee, J. H., Jan. 2004. Spectrum of a Leonid meteor from 110 to 860 nm. Advances in Space Research 33, 1455–1458.

Ceplecha, Z., Revelle, D. O., Jan. 2005. Fragmentation model of meteoroid motion, mass loss, and radiation in the atmosphere. Meteoritics and Planetary Science 40, 35.

Charriet, M., Fayolle, G., Dec. 2013. Projet de Nanosatellite à l'UPMC. Master's thesis, Université Pierre et Marie Curie, Paris, France.

676 Christou, A. A., Oberst, J., Elgner, S., Flohrer, J., Margonis, A., McAuliffe, J. P.,
677 Koschny, D., Jan. 2012. Orbital observations of meteors in the Martian atmo-
678 sphere using the SPOSH camera. Planetary and Space Science 60, 229–235.

679 Ebisuzaki, T., Mase, H., Takizawa, Y., Kawasaki, Y., Miyamoto, H., Shinozaki,
680 K., Ohmori, H., Hachisu, H., Wada, S., Ogawa, T., Kajino, F., Inoue, N.,
681 Sakaki, N., Adams, J., Christl, M., Young, R., Bonamente, M., Santangelo,
682 A., Teshima, M., Parizot, E., Gorodetzky, P., Catalano, O., Picozza, P., Ca-
683 solino, M., Bertaina, M., Panasyuk, M., Khrenov, B. A., Park, I. H., Neronov,
684 A., Medina-Tanco, G., Rodriguez-Frias, D., Szabelski, J., Bobik, P., Tsenov,
685 R., Sep. 2011. The JEM-EUSO Mission. In: Sagawa, H., Kawasaki, Y., Sako,
686 T., Takeda, M., Tsunesada, Y. (Eds.), American Institute of Physics Confer-
687 ence Series. Vol. 1367 of American Institute of Physics Conference Series. pp.
688 120–125.

689 Gritsevich, M., Koschny, D., Apr. 2011. Constraining the luminous efficiency of
690 meteors. Icarus 212, 877–884.

691 Gritsevich, M. I., Dec. 2007. Approximation of the observed motion of bolides
692 by the analytical solution of the equations of meteor physics. Solar System
693 Research 41, 509–514.

694 Gritsevich, M. I., Oct. 2008. The Pribram, Lost City, Innisfree, and
695 Neuschwanstein falls: An analysis of the atmospheric trajectories. Solar System
696 Research 42, 372–390.

697 Gritsevich, M. I., Aug. 2009a. Determination of parameters of meteor bodies
698 based on flight observational data. Advances in Space Research 44, 323–334.

699 Gritsevich, M. I., Aug. 2009b. Determination of parameters of meteor bodies
700 based on flight observational data. Advances in Space Research 44, 323–334.

701 Gritsevich, M. I., Stulov, V. P., Dec. 2006. Extra-atmospheric masses of the Cana-
702 dian Network bolides. Solar System Research 40, 477–484.

703 Gritsevich, M. I., Stulov, V. P., Turchak, L. I., Feb. 2012. Consequences of colli-
704 sions of natural cosmic bodies with the Earth's atmosphere and surface. Cosmic
705 Research 50, 56–64.

706 Grun, E., Zook, H. A., Fechtig, H., Giese, R. H., May 1985. Collisional balance
707 of the meteoritic complex. Icarus 62, 244–272.

708 Halliday, I., Blackwell, A. T., Griffin, A. A., Feb. 1978. The Innisfree meteorite
709 and the Canadian camera network. Journal of the Royal Astronomical Society
710 of Canada 72, 15–39.

711 Halliday, I., Griffin, A. A., Blackwell, A. T., Oct. 1981. A photometric study of the
712 Innisfree meteorite fall. Journal of the Royal Astronomical Society of Canada
713 75, 247–248.

714 Halliday, I., Griffin, A. A., Blackwell, A. T., Mar. 1996. Detailed data for 259 fire-
715 balls from the Canadian camera network and inferences concerning the influx
716 of large meteoroids. Meteoritics and Planetary Science 31, 185–217.

717 Hunt, S. M., Oppenheim, M., Close, S., Brown, P. G., McKeen, F., Minardi, M.,
718 Mar. 2004. Determination of the meteoroid velocity distribution at the Earth
719 using high-gain radar. Icarus 168, 34–42.

720 Jenniskens, P., Gural, P. S., Dynneson, L., Grigsby, B. J., Newman, K. E., Borden,
721 M., Koop, M., Holman, D., Nov. 2011. CAMS: Cameras for Allsky Meteor
722 Surveillance to establish minor meteor showers. Icarus 216, 40–61.

723 Koschny, D., McAuliffe, J., Jan. 2009. Estimating the number of impact flashes
724 visible on the Moon from an orbiting camera. Meteoritics and Planetary Science
725 44, 1871–1875.

726 Mimoun, D., Wieczorek, M. A., Alkalai, L., Banerdt, W. B., Baratoux, D.,
727 Bougeret, J.-L., Bouley, S., Cecconi, B., Falcke, H., Flohrer, J., Garcia, R. F.,
728 Grimm, R., Grott, M., Gurvits, L., Jaumann, R., Johnson, C. L., Knapmeyer,
729 M., Kobayashi, N., Konovalenko, A., Lawrence, D., Feuvre, M. L., Lognonné,
730 P., Neal, C., Oberst, J., Olsen, N., Röttgering, H., Spohn, T., Vennerstrom, S.,
731 Woan, G., Zarka, P., Apr. 2012. Farside explorer: unique science from a mission
732 to the farside of the moon. Experimental Astronomy 33, 529–585.

733 Nemtchinov, I. V., Popova, O. P., Shuvalov, V. V., Svetsov, V. V., Jun. 1994. Radi-
734 ation emitted during the flight of asteroids and comets through the atmosphere.
735 Planetary and Space Science 42, 491–506.

736 Oberst, J., Flohrer, J., Elgner, S., Maue, T., Margonis, A., Schrödter, R., Tost,
737 W., Buhl, M., Ehrich, J., Christou, A., Koschny, D., Jan. 2011. The Smart
738 Panoramic Optical Sensor Head (SPOSH)A camera for observations of tran-
739 sient luminous events on planetary night sides. Planetary and Space Science
740 59, 1–9.

741 Oberst, J., Lainey, V., Le Poncin-Lafitte, C., Dehant, V., Rosenblatt, P., Ulamec,
742 S., Biele, J., Spurmann, J., Kahle, R., Klein, V., Schreiber, U., Schlicht, A.,

743 Rambaux, N., Laurent, P., Noyelles, B., Foulon, B., Zakharov, A., Gurvits, L.,
744 Uchaev, D., Murchie, S., Reed, C., Turyshev, S. G., Gil, J., Graziano, M., Will-
745 ner, K., Wickhusen, K., Pasewaldt, A., Wählisch, M., Hoffmann, H., Oct. 2012.
746 GETEMME, a mission to explore the Martian satellites and the fundamentals
747 of solar system physics. Experimental Astronomy 34, 243–271.

748 Oberst, J., Molau, S., Heinlein, D., Gritzner, C., Schindler, M., Spurny, P., Ce-
749 plecha, Z., Rendtel, J., Betlem, H., Jan. 1998. The "European Fireball Net-
750 work": Current status and future prospects. Meteoritics and Planetary Science
751 33, 49–56.

752 Rendtel, J., 2004. The population index of sporadic meteors. In: Triglav-Čekada,
753 M., Trayner, C. (Eds.), Proceedings of the International Meteor Conference,
754 22nd IMC, Bollmannsruh, Germany, 2003. pp. 114–122.

755 Revelle, D. O., Ceplecha, Z., Nov. 2001. Bolide physical theory with application
756 to PN and EN fireballs. In: Warmbein, B. (Ed.), Meteoroids 2001 Conference.
757 Vol. 495 of ESA Special Publication. pp. 507–512.

758 Trigo-Rodríguez, J. M., Castro-Tirado, A. J., Llorca, J., Fabregat, J., Martínez,
759 V. J., Reglero, V., Jelínek, M., Kubánek, P., Mateo, T., Postigo, A. D. U., Dec.
760 2004. The Development of the Spanish Fireball Network Using a New All-Sky
761 CCD System. Earth Moon and Planets 95, 553–567.

762 Vaubaillon, J., Koten, P., Rudawska, R., Bouley, S., Maquet, L., Colas, F., Toth,
763 J., Zender, J., McAuliffe, J., Pautet, D., Jenniskens, P., Gerding, M., Borovicka,
764 J., Koschny, D., Leroy, A., Lecacheux, J., Gritsevich, M., Duris, F., Jan. 2013.
765 Overview of the 2011 Draconids airborne observation campaign. In: Gyssens,

766 M., Roggemans, P. (Eds.), Proceedings of the International Meteor Conference,
767 31st IMC, La Palma, Canary Islands, Spain, 2012. pp. 61–64.

768 Verniani, F., Aug. 1966. Meteor Masses and Luminosity. SAO Special Report
769 219.

770 Wetherill, G. W., Revelle, D. O., Nov. 1981. Which fireballs are meteorites - A
771 study of the Prairie Network photographic meteor data. Icarus 48, 308–328.

Table 1: Symbols and parameters used in this paper

Symbol	Unit	Expression/Value	Meaning
α	-	$0.5 c_d \frac{\rho_0 h_0 S_e}{M_e sin\gamma}$	Ballistic coefficient
β	-	$0.5(1-\mu)\frac{c_h {V_e}^2}{c_d H*}$	Mass loss coefficient
σ	s^2/m^2	$\frac{2\beta}{(1-\mu){V_e}^2}$	Ablation coefficient. Note: 100σ is more often used.
γ	degrees	-	Slope between horizon and trajectory
ρ_0	kg/m^3	-	Atmospheric density at sea level
ρ_{atmos}	kg/m^3	-	Atmospheric density
ρ_m	kg/m^3	-	Meteoroid bulk density.
A_e	-	$\frac{S_e \rho_m^{2/3}}{{M_e}^{2/3}}$	Meteoroid initial shape factor
A	-	$\frac{S \rho_m^{2/3}}{M^{2/3}}$	Meteoroid shape factor
c_d	-	-	Drag coefficient
c_h	-	-	Heat transfer coefficient
h	km	-	Height of meteoroid
h_0	km	7.16	Scale height of atmosphere
$\bar{h}$	-	h/h_0	Dimensionless height of meteoroid
H^*	J/kg	-	Effective destruction enthalpy
I	W	-	Luminous intensity of meteor
E_{kin}	J	$0.5MV^2$	Kinetic energy of meteor
$E_{kin,e}$	J	$0.5M_eV_e^2$	Initial kinetic energy of meteor
E_{lum}	J	–	Total luminous energy of meteor
M	kg or g	–	Meteoroid Mass
M_e	kg or g	–	Initial meteoroid Mass
$\bar{M}$	-	M/M_e	Dimensionless mass of meteoroid
M_{phot}	kg or g	-	Mass of meteoroid evaluated by photometric method
V	km/s	–	Meteoroid velocity
V_e	km/s	–	Initial meteoroid velocity
$\bar{V}$	-	V/V_e	Dimensionless meteoroid velocity
μ	-	-	Shape change coefficient
τ	-	$I/\frac{dE_{kin}}{dt}$	Luminous efficiency
τ_{global}	-	$\frac{E_{lum}}{E_{kin,e}}$	Global luminous efficiency
S	m^2	-	Cross-section area
S_e	m^2	-	Initial cross-section area

Table 2: Main characteristics of the SPOSH camera, according to Oberst et al. (2011)

Characteristic	Value
Maximum apparent magnitude of detectable object	6
Maximum angular speed of object	$5^\circ/\mathrm{s}$
Field of view	120° x 120°
Minimum exposure time	0.06 s

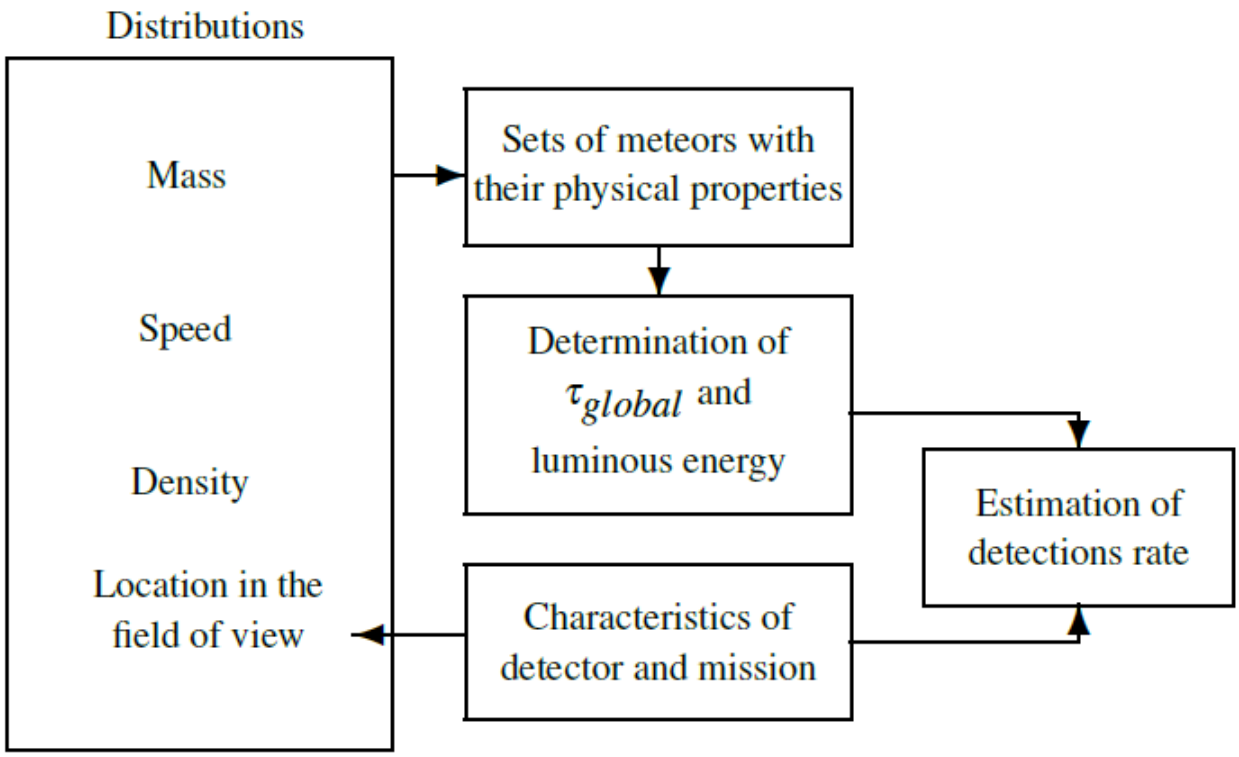

Figure 1: Architecture of the simulator

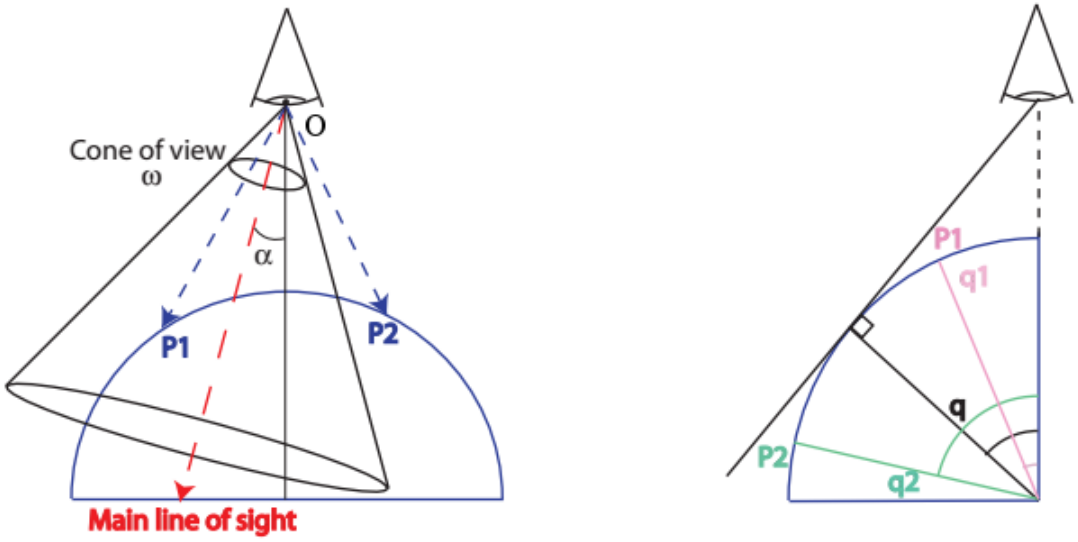

Figure 2: Discrimination of points included in field of view. On the left: For each point P_i, the value of scalar product of $\vec{OP_i}$ with the unitary vector along the main line of sight permits to find the angle between the two and whether P_i is included within the field of view. On the right: The angle θ for a point at horizon depends on detector altitude but is independent of the angle of the line of sight. Once it is calculated, each point P_i verifying $\theta_i > \theta$ is beyond the horizon and must be eliminated.

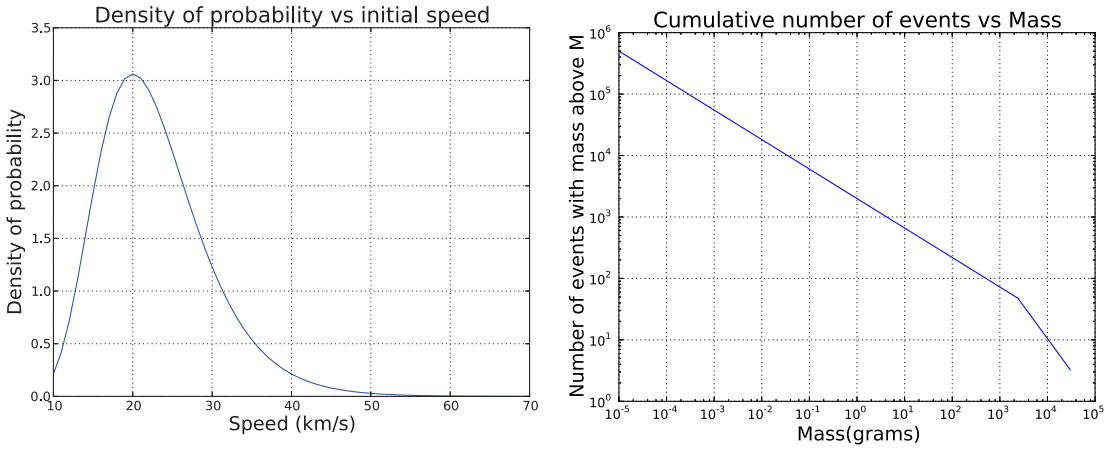

Figure 3: Distributions adopted in initial speeds and initial masses of meteoroids.

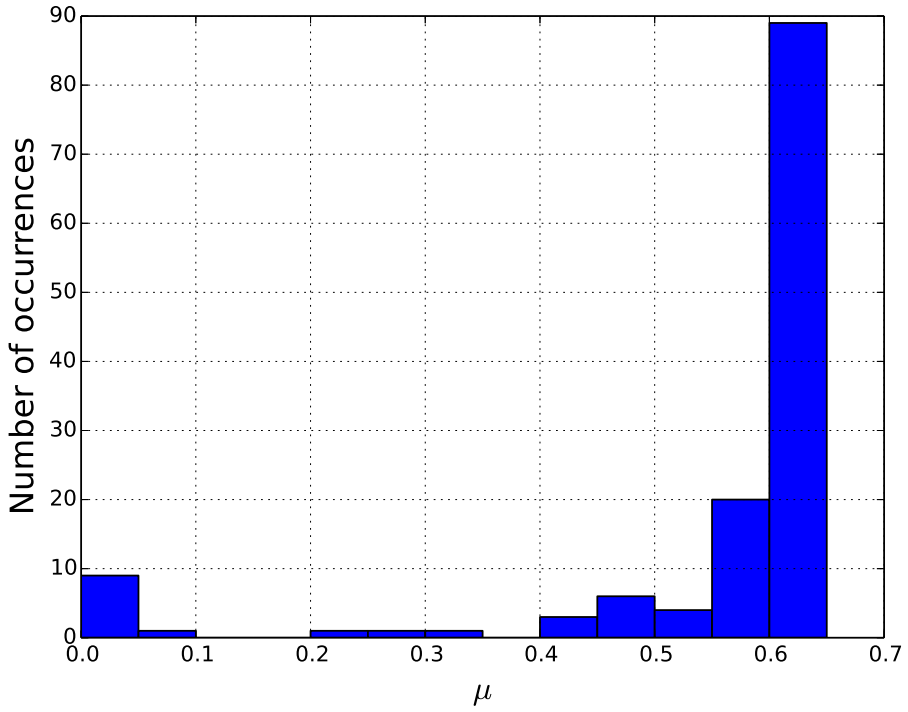

Figure 4: Distribution of values of shape change coefficient μ found through fitting to the light curve in the Canadian Network meteors. 0.65 corresponds to homogeneous distribution of heat by rotation around the meteoroid.

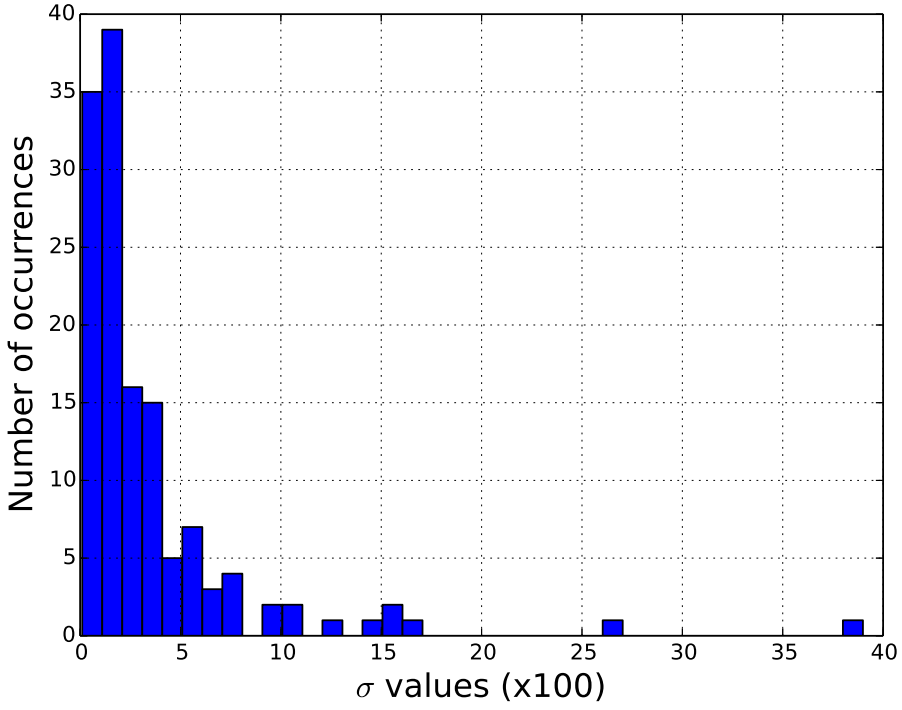

Figure 5: Distribution of values of σ in the Canadian Network meteors.

Figure 6: The SPOSH camera

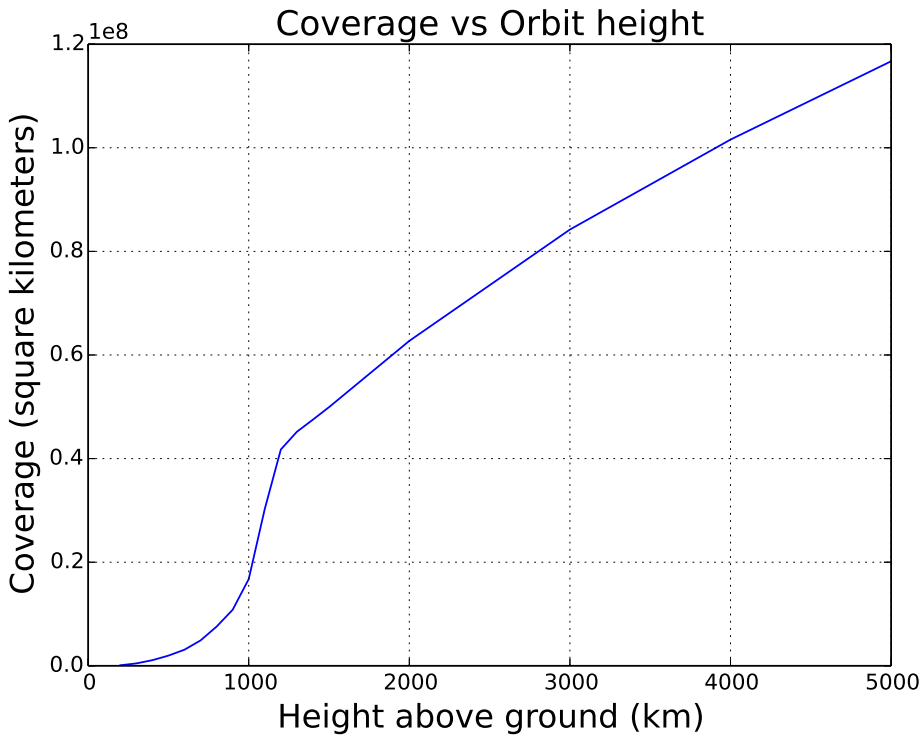

Figure 7: Coverage as a function of orbit height, for a SPOSH camera pointed toward nadir.

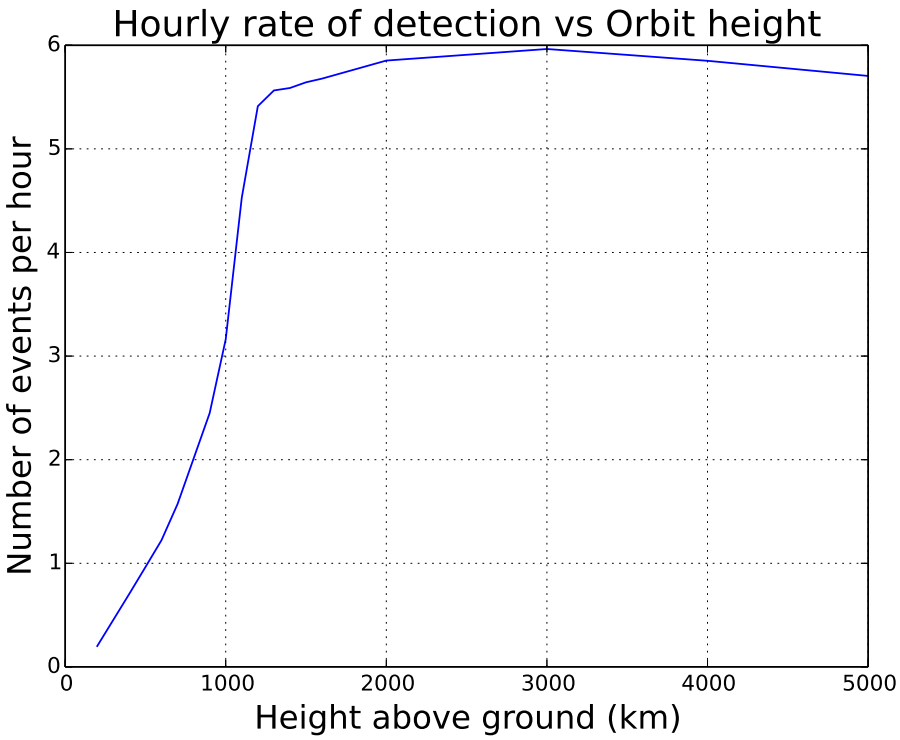

Figure 8: Evolution of hourly rate of detection by a SPOSH camera pointed towards nadir, as a function of orbit height

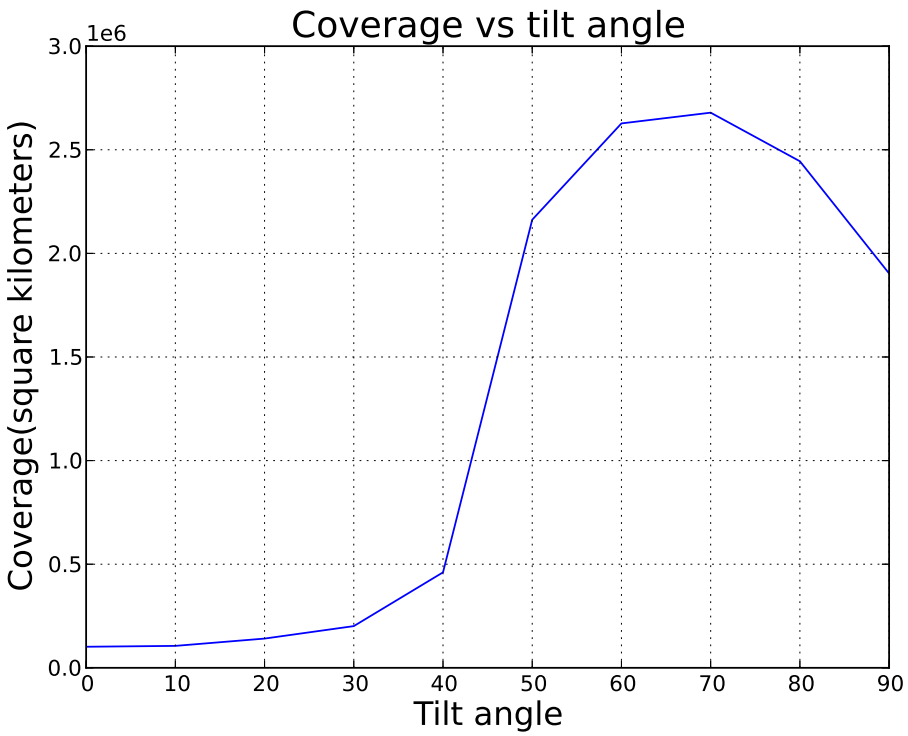

Figure 9: Evolution of coverage by JEM-EUSO as a function of angle of tilt.

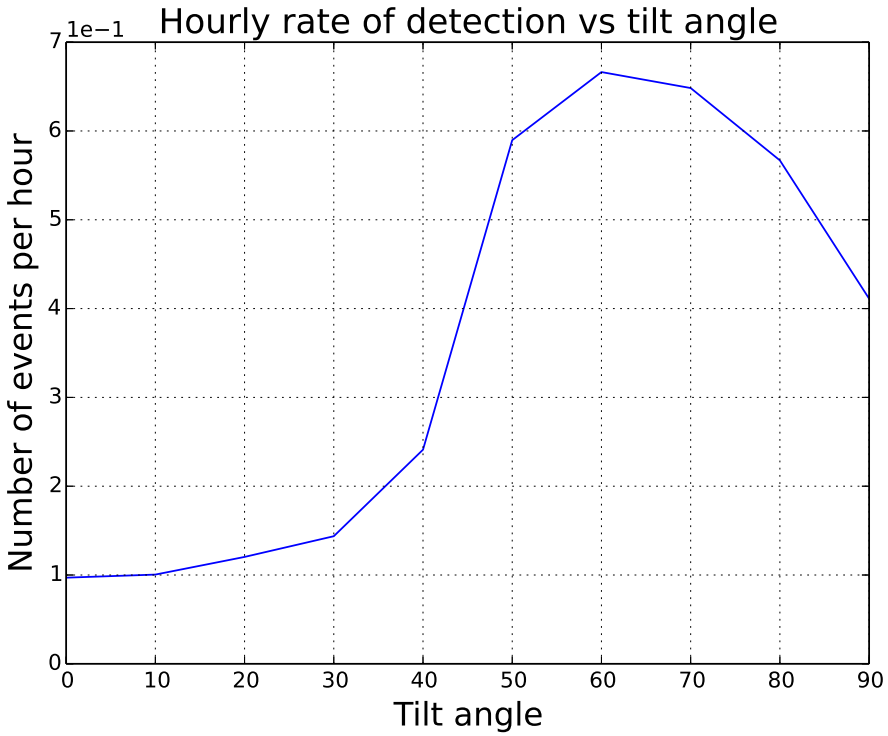

Figure 10: Evolution of hourly rate of detection by JEM-EUSO as a function of angle of tilt.

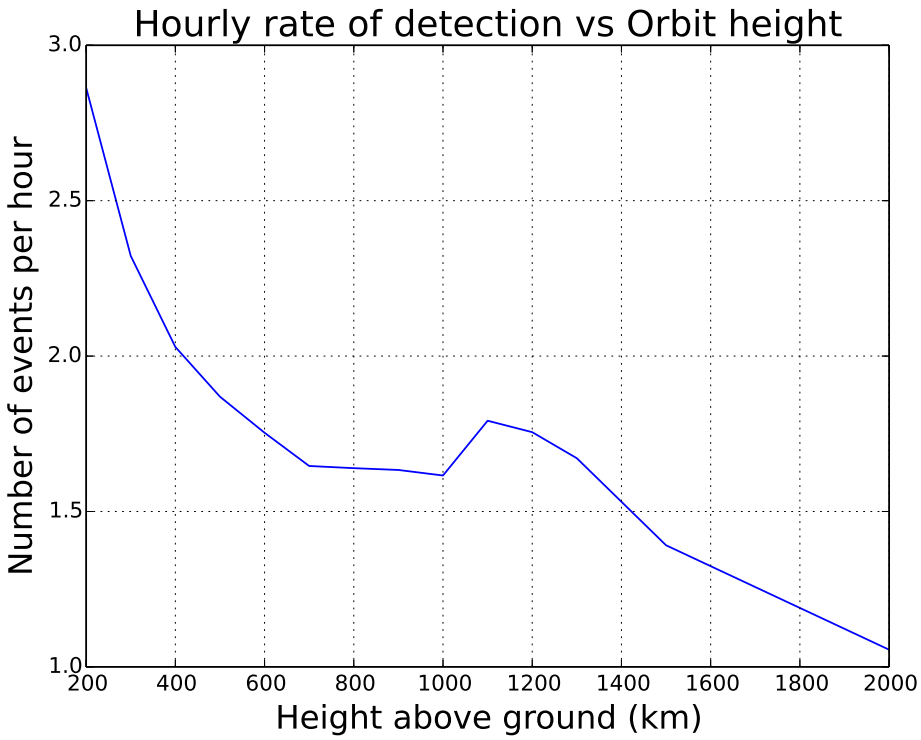

Figure 11: Evolution of hourly rate of detection by a SPOSH camera, assuming a mass index of 2.17, as a function of orbit height